PCCP

PAPER

View Article Online
View Journal | View Issue

Cite this: *Phys. Chem. Chem. Phys.*, 2026, **28**, 3907

CO_2 photoreduction on mixed Ti/Zr-MOF-525: bicarbonate as the active intermediate and the role of Ti substitution

Thanyaporn Puengpoka,[a] Jirapat Santatiwongchai,[b] Warot Chotpatiwetchkul,*[a] Sareeya Bureekaew,[c] Muhammad Saleh,[d] Anchalee Junkaew[b] and Sarawoot Impeng*[b]

Received 30th October 2025,
Accepted 7th January 2026

DOI: 10.1039/d5cp04190b

rsc.li/pccp

The photocatalytic reduction of CO_2 in metal–organic frameworks (MOFs) offers a sustainable route to C_1 fuels and chemicals. Herein, density functional theory (DFT) calculations elucidate CO_2 reduction on mixed Ti/Zr-MOF-525 clusters bearing missing linker defects, modeled by Zr_6, Ti_1Zr_5, and Ti_2Zr_4 clusters. Two distinct mechanistic pathways are identified: the OH-passive and OH-assisted routes. In the passive case, CO_2 binds weakly at a coordinatively unsaturated Ti/Zr site and undergoes direct hydrogenation to CO and HCOOH, with desorption being thermodynamically preferred over further hydrogenation. In contrast, the OH-assisted pathway proceeds *via* a bicarbonate-mediated mechanism, where surface –OH attacks adsorbed CO_2 to form node-bound $*HCO_3$. This step is both thermodynamically favorable and kinetically accessible ($\Delta G^{\ddagger} < 0.5$ eV). Subsequent proton-electron additions convert $*HCO_3$ to *OCHO and H_2O, favored by $\sim$1 eV over competing routes. These findings identify $*HCO_3$ as the true reactive precursor and reveal that Ti substitution promotes deeper hydrogenation beyond two-electron products, enhancing CH_4 formation on the Ti_2Zr_4 cluster. Overall, the results highlight the importance of node composition and surface hydroxyl groups in porphyrinic MOFs for optimizing multi-electron CO_2 reduction and controlling product selectivity by tailoring the metal node environments.

Introduction

Carbon dioxide (CO_2) is a major greenhouse gas driving global warming and climate change. Reducing CO_2 emissions is thus an urgent challenge on the path toward achieving carbon neutrality. Carbon capture and utilization (CCU) has emerged as a promising strategy because it simultaneously lowers atmospheric CO_2 levels and upcycles this abundant C_1 feedstock into valuable chemicals and fuels, such as carbon monoxide (CO), formic acid (HCOOH), methanol (CH_3OH), and methane (CH_4).[1–4] CO_2 can be converted *via* thermocatalysis, electrocatalysis, photocatalysis, and photoelectrochemical or biochemical pathways.[4] Among these, photocatalytic CO_2 reduction is particularly attractive because it directly harnesses solar energy under mild operating conditions, providing a sustainable route to close the carbon cycle and produce renewable fuels.[5,6]

A wide range of photocatalysts have been explored for solar-driven CO_2 conversion, including molecular complexes, noble-metal nanoparticles, organic polymers, inorganic semiconductors, and hybrid materials.[6,7] However, these systems often suffer from limited stability, modest selectivity, and inefficient charge separation, highlighting the need for improved photocatalyst design. Metal–organic frameworks (MOFs) have emerged as a versatile class of photocatalysts for CO_2 reduction.[6,8,9] Their high surface areas, tunable porosity, adjustable chemical composition, and engineerable electronic structures make them well-suited for light-driven catalysis. From the fundamentals of CO_2 photocatalysis, an efficient photocatalyst should combine (i) strong absorption in the visible-light region (bandgap $\leq$ 3 eV), (ii) long-lived excited states, (iii) efficient charge generation and separation, (iv) high charge mobility, and (v) strong CO_2 adsorption capacity.[2,5,6] MOFs are uniquely positioned to integrate these features within a single material, placing them among the most promising candidates for next-generation photocatalyst design. Within this family, porphyrinic MOFs are especially compelling because their strong visible-light absorption and well-defined, modular

[a] *Applied Computational Chemistry Research Unit, Department of Chemistry, School of Science, King Mongkut's Institute of Technology Ladkrabang, Bangkok, Thailand. E-mail: warot.ch@kmitl.ac.th*
[b] *National Nanotechnology Center (NANOTEC), National Science and Technology Development Agency (NSTDA), Pathum Thani 12120, Thailand. E-mail: sarawoot.imp@nanotec.or.th*
[c] *Department of Chemical and Biomolecular Engineering, School of Energy Science and Engineering, Vidyasirimedhi Institute of Science and Technology, Rayong 21210, Thailand*
[d] *Lehrstuhls für Theoretische Physik elektrifizierter Flüssig-Festkörper-Grenzflächen Ruhr-Universität Bochum Universitätsstraße 150, 44801 Bochum, Germany*

catalytic environments directly address these fundamental requirements for efficient CO_2 photoreduction.[10,11]

Within this subclass, particular attention has been paid to Zr-porphyrinic frameworks such as MOF-525 and MOF-545, which have emerged as especially promising candidates. Both structures consist of tetrakis(4-carboxyphenyl)porphyrin (TCPP) linkers connected to Zr_6-oxo clusters, but they commonly exhibit distinct product selectivity: MOF-525 tends to yield CO and CH_4, whereas MOF-545 more often favors formate.[12,13] Their photocatalytic performance can be further enhanced through porphyrin metalation or partial Ti^{4+} substitution at the Zr_6 node.[14–16] In MOF-525, Ti incorporation can enhance charge separation and enable partial reduction of Ti^{4+} to Ti^{3+} under light irradiation, generating electron-rich sites that stabilize key intermediates and promote deeper hydrogenation toward CH_4.[16] Crucially, catalytic activity is governed by the availability of open metal sites (OMS); increasing their density and accessibility enhances CO_2 adsorption and subsequent conversion, thereby enhancing overall catalytic performance. In this regard, hydroxyl-capped missing-linker defects increase the density and accessibility of Zr/Ti OMS, which serve as active sites that (i) directly bind and activate CO_2 for stepwise hydrogenation or (ii) facilitate nucleophilic attack by neighboring surface OH groups on adsorbed CO_2 to form carbonate-like intermediates. Similar Zr^{3+}–OH frustrated Lewis pairs (FLPs) have been identified as active sites for CO_2 activation in UiO-66,[17] suggesting analogous behavior in porphyrinic MOFs. In addition, spectroscopic and computational studies have shown that photoexcitation of the porphyrin linker can induce linker-to-node charge transfer to the inorganic node, the catalytic center.[12,16,18,19] Collectively, the interplay between node composition, defect chemistry (*via* OMS and FLPs), and linker-node charge transfer collectively dictates the reaction mechanism and product selectivity in photocatalytic CO_2 reduction.

Despite these advances, the mechanistic roles of Ti substitution and surface –OH groups at defect sites in controlling product selectivity remain insufficiently understood. Herein, density functional theory (DFT) calculations are employed to investigate CO_2 photoreduction on mixed Ti/Zr-MOF-525 clusters bearing missing linker defects. Finite-cluster models containing missing-linker defects capped by $-OH/H_2O$ ligands are constructed to represent catalytically relevant environments. Two mechanistic pathways are examined: an OH-passive pathway, in which hydroxyl groups act as spectators, and an OH-assisted pathway, where hydroxyl groups directly attack the adsorbed CO_2 to form carbonate-like intermediates that promote subsequent hydrogenation steps. By systematically comparing Zr_6, Ti_1Zr_5, and Ti_2Zr_4 clusters, we map the free-energy landscape to reveal how Ti substitution and hydroxyl defects modulate reaction energetics and product selectivity, providing mechanistic design guidelines for efficient MOF-based photocatalysts.

Computational details

We employed a finite-cluster model to study CO_2 photoreduction on mixed Ti/Zr-MOF-525 containing missing-linker defects. The Zr_6-oxo cluster was extracted from the experimental MOF-525 crystal structure.[20] One tetrakis(4-carboxyphenyl)porphyrin (TCPP) linker was removed to create a missing-linker defect, resulting in undercoordinated Zr centers. These sites were initially capped with hydroxyl (–OH) and water (H_2O) ligands to restore coordination and maintain charge neutrality. To generate the catalytically active site, one H_2O ligand was then removed, creating an open (coordinatively unsaturated) metal center at Zr or Ti (for substituted clusters). The remaining porphyrin linkers were truncated and capped with acetate groups, following our previous protocol,[21,22] which preserves the local electronic structure of the node and adsorption energetics in cluster models. Ti substitution was introduced at the defect-centered node by replacing one or two Zr atoms, yielding three catalyst models denoted as Zr_6-, Ti_1Zr_5-, and Ti_2Zr_4-MOF-525, respectively. These clusters allow a direct evaluation of the role of Ti substitution on product selectivity and the participation of hydroxyl groups in the reaction mechanism. The constructed cluster models are shown in Fig. 1.

Spin-unrestricted DFT calculations were performed with the M06-L functional[23] using Gaussian 16.[24] Stuttgart–Dresden (SDD) effective core potentials with associated basis sets were applied to Zr and Ti,[25] while the def2-SVP basis set was used for C, H, and O during geometry optimizations.[26] Single-point energy refinements were carried out with the def2-TZVP basis set on non-metal atoms, including Grimme's D3 dispersion correction[27] and the SMD implicit solvation model[28] (water as solvent) to account for long-range dispersion and solvent stabilization effects. During optimization, the carboxylate carbon atoms of acetate caps were constrained, whereas all other atoms were fully relaxed.

Harmonic frequency calculations at the M06-L/def2-SVP level provided zero-point and thermal corrections. Low-frequency vibrational modes were treated using a Truhlar-type quasi-harmonic correction[29] implemented in the GoodVibes program,[30] applying a 100 cm^{-1} cutoff and a vibrational scaling factor of 0.976 for thermochemical analysis. All reported energies are Gibbs free

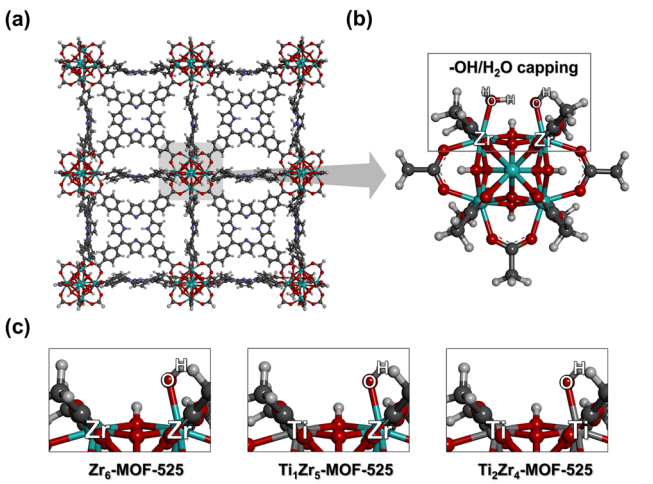

Fig. 1 Structural representation of MOF-525: (a) pristine framework, (b) cluster model with $-OH/H_2O$ capping at a missing linker defect, and (c) mixed Ti/Zr-MOF-525 showing Ti substitution at the metal node and the formation of Zr/Ti open sites upon H_2O removal. Zr, Ti, O, N, C and H atoms are shown in cyan, gray, red, blue, dark gray and white, respectively.

energies at 298.15 K and 1 atm. The Gibbs free energy change for the proton-coupled electron transfer (PCET) steps was calculated using the computational hydrogen electrode (CHE) approach.[31] In this method, the free energy of the proton-electron pair ($H^+ + e^-$) is defined as half of the free energy of molecular hydrogen in the gas phase.

Results and discussion

As reported elsewhere,[16,32] two mechanistic pathways were considered depending on the involvement of the surface hydroxyl group: (i) the OH-passive pathway, in which the hydroxyl group remains chemically inactive, and (ii) the OH-assisted pathway, where the hydroxyl group directly interacts with the adsorbed CO_2. The corresponding elementary steps for both mechanisms are illustrated in Scheme 1, and their reaction energetics are discussed in the following subsections.

OH-passive pathway

In the OH-passive pathway, the surface hydroxyl group remains chemically inert and does not take part in the reaction. The reduction begins with CO_2 adsorption at a coordinatively unsaturated Zr/Ti site. Fig. 2 presents the calculated Gibbs free-energy profiles for CO_2 photoreduction on Zr_6-, Ti_1Zr_5-, and Ti_2Zr_4-MOF-525 clusters, together with their optimized structures along the reaction pathway (Fig. S1). Two hydrogenation pathways were evaluated: (i) the formate pathway, producing the surface-bound *OCHO, and (ii) the carboxyl route, proceeding through *COOH. The adsorbed CO_2 molecule remains nearly linear, with an O–C–O bond angle of around 170°, indicating that its geometry is largely preserved upon adsorption. This small deviation from linearity reflects weak physisorption and minimal charge transfer to the Lewis-acidic Zr/Ti center, consist with the small positive Mulliken charge on the adsorbed CO_2 (around $+0.1|e|$). The calculated Gibbs free energies of CO_2 adsorption (0.32–0.41 eV) are positive, confirming weak, non-activated adsorption at the Zr/Ti sites.

The first proton–electron transfer step protonates the adsorbed CO_2 to generate either *OCHO or *COOH and is thermodynamically uphill by around 2.5 eV for all models, revealing that CO_2 activation on OH-passive surfaces is highly unfavorable. The large barrier originates from the limited electron-accepting ability of the neutral Zr^{4+}/Ti^{4+} centers, which

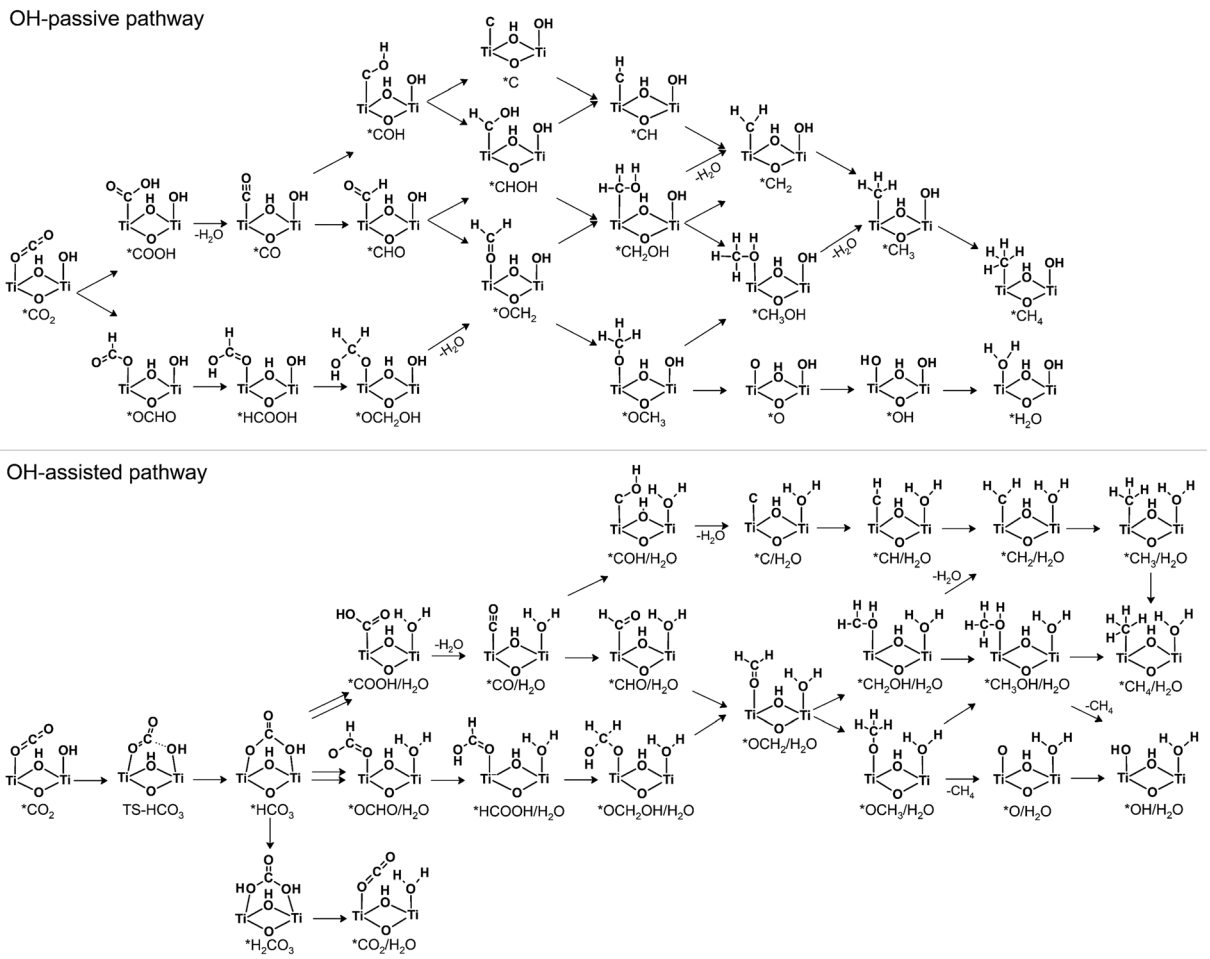

Scheme 1 Proposed OH-passive and OH-assisted pathways for CO_2 reduction on mixed Ti/Zr-MOF-525 clusters, illustrated using a simplified Ti_2Zr_4 model representative of the mechanisms studied across Zr_6, Ti_1Zr_5, and Ti_2Zr_4 clusters.

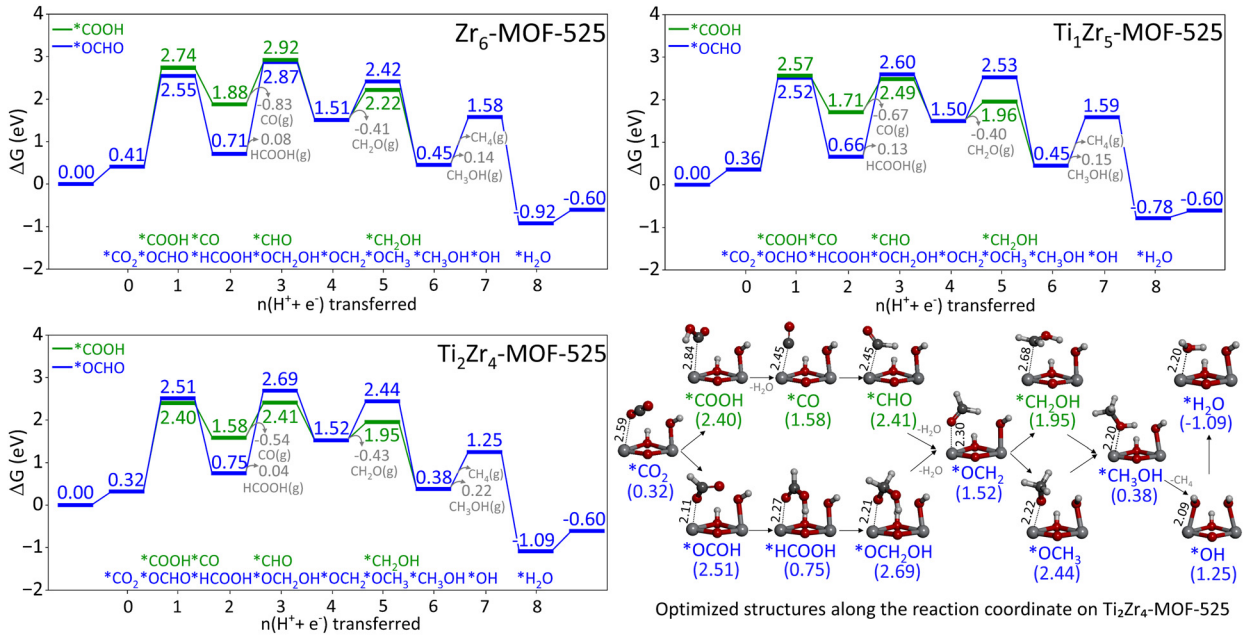

Fig. 2 Gibbs free-energy profiles (Δ*G*, eV) for the OH-passive pathway on Zr_6-, Ti_1Zr_5-, and Ti_2Zr_4-MOF-525 clusters. The reactant state (MOF + CO_2) is used as the energy reference, and water desorption regenerates the active site. Optimized structures along the reaction coordinate are shown for the Ti_2Zr_4-MOF-525, while those for Zr_6- and Ti_1Zr_5-MOF-525 are provided in the SI.

restricts charge transfer to CO_2 and hinders its reduction. Under photocatalytic conditions, partial reduction of the node metal to Zr^{3+}/Ti^{3+} could promote electron donation to CO_2 and facilitate activation; however, our neutral state results describe the intrinsic thermodynamic character of OH-passive sites prior to photoinduced charge transfer.

Hydrogenation of *COOH produces *CO, completing the two-electron reduction sequence. For *CO, two protonation channels were examined, formation of *CHO or *COH. The *CHO intermediate is more stable by $>$ 1 eV than *COH (Table S1), whereas *COH is intrinsically unstable and reacts with a neighboring surface –OH to give a $C(OH)_2$-like species (Fig. S1). Thus, *COH cannot exist as an isolated intermediate under OH-passive conditions. All such high-energy or spontaneously reacting species are depicted in gray in Fig. S1 and Table S1 to indicate their minor mechanistic relevance.

Hydrogenation of *OCHO, in contrast, yields *HCOOH, which is thermodynamically more stable than *CHO for all catalysts. Further protonation converts *HCOOH to $*OCH_2OH$ and subsequent hydrogenation of either $*OCH_2OH$ or *CHO produces $*OCH_2$ (Fig. 2).

Both formate and carboxyl pathways therefore merge at OCH_2, a common precursor to CH_3OH and CH_4.

However, desorption of the C_1 products CO and HCOOH is thermodynamically more favorable than continued hydrogenation. The computed free energies of CO desorption are −0.83, −0.67, and −0.54 eV for Zr_6, Ti_1Zr_5, and Ti_2Zr_4 clusters, respectively, indicating that CO is already released from the surfaces. HCOOH desorption is slightly endergonic ($\sim$0.1 eV, suggesting that it can also desorb under mild conditions. Because both CO and HCOOH desorption are preferred over additional hydrogenation, the CO_2 reduction process on OH-passive nodes terminates at these two-electron products. This result emphasizes that, in the absence of surface-OH participation, reduction at Zr/Ti sites is confined to CO and HCOOH formation, underscoring the necessity of local reactivity –OH environments for achieving deeper multi-proton–electron conversions.

Experimentally, deeper hydrogenation to CH_4 has been observed for mixed Ti/Zr-MOF-525 catalysts,[16] likely due to photoinduced charge transfer and active OH sites that enhance CO_2 activation and promote multi-electron processes. The following section therefore examines the OH-assisted pathway, where surface hydroxyl groups directly engage in CO_2 activation.

OH-assisted pathway

As in the passive pathway, CO_2 first adsorbs at a coordinatively unsaturated Zr/Ti site. In contrast, the OH-assisted mechanism involves the direct participation of the surface –OH, which attacks the adsorbed CO_2 carbon to form a node-bound bicarbonate ($*HCO_3$) species. This step represents a Lewis acid–base activation, where the surface –OH acts as a Lewis base and the Zr/Ti site as a Lewis acid. No proton–electron transfer occurs at this stage; the actual reduction begins only after $*HCO_3$ formation.

Fig. 3 presents the calculated Gibbs free-energy profiles for CO_2 photoreduction on Zr_6-, Ti_1Zr_5-, and Ti_2Zr_4-MOF-525 clusters, together with their optimized structures along the reaction pathway (Fig. S2). All high-energy intermediates are shown in gray in Fig. S2 and listed in Table S2 to indicate their minor mechanistic significance. At the transition state, the OH approaches the CO_2 carbon, forming a partial $O_{(OH)}$–C bond, elongating both C–O bonds, and bending the O–C–O angle further from linearity. The transition state exhibits single imaginary frequencies of 166.2*i*,

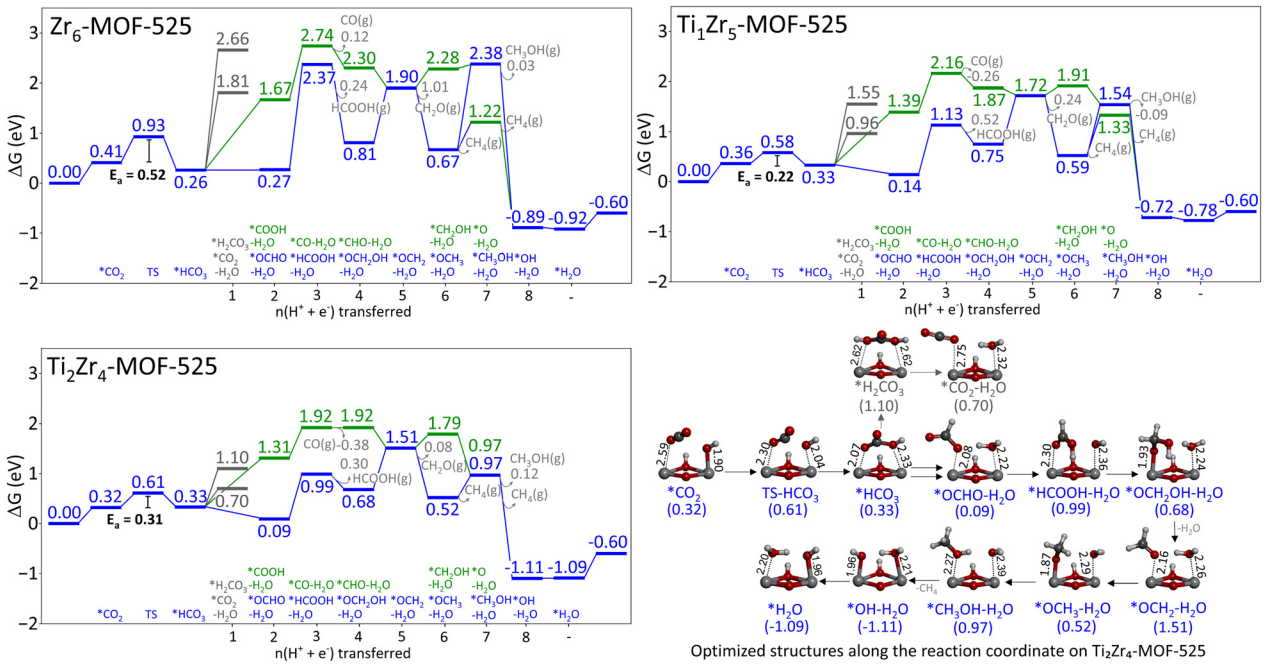

Fig. 3 Gibbs free-energy profile (ΔG, eV) for the OH-assisted pathway on Zr_6-, Ti_1Zr_5-, and Ti_2Zr_4-MOF-525 clusters. The reactant state (MOF + CO_2) is used as the energy reference, and water desorption regenerates the active site. Optimized structures along the reaction coordinate are shown for Ti_2Zr_4-MOF-525, while those for Zr_6- and Ti_1Zr_5-MOF-525 are provided in the SI.

269.4i, and 295.5i cm^{-1} for Zr_6, Ti_1Zr_5, and Ti_2Zr_4, respectively. The reaction is slightly endergonic ($\sim$0.3 eV) with activation free energies of 0.52, 0.22, and 0.31 eV for Zr_6, Ti_1Zr_5, and Ti_2Zr_4, respectively, demonstrating that Ti substitution markedly lowers the OH-attack barrier.

Charge and structural analyses clarify this effect (Table 1). In the Zr_6 system, charge accumulation resides on the metal (Δq(M) = $-0.14|e|$) with negligible O $\rightarrow$ C ($\sim 0|e|$), yielding a moderately bent CO_2 (O–C–O = 155.8°) and a long $O_{(OH)}$–C distance (2.04 Å), consistent with the highest activation barrier (0.52 eV). In Ti_1Zr_5, a slight positive shift in Δq(M) (+0.01$|e|$) indicates Ti-induced polarization of the Zr–OH site, enabling limited donation into CO_2 π^* orbitals. Consequently, CO_2 bends more (149.5°) and the $O_{(OH)}$–C distance shortens (1.87 Å), reducing the activation free energy to 0.22 eV.

Table 1 Charge redistribution, activation Gibbs free energy ($\Delta G^{\ddagger}$), and CO_2 geometry along the OH-assisted pathway. $\Delta q = q$(TS) $- q$(ADS); Δq in $|e|$; $\Delta G^{\ddagger}$ in eV; O–C–O in degrees

System	Δq_$C_{(CO_2)}$ $\lvert e\rvert$	Δq_$O_{(OH)}$ $\lvert e\rvert$	Δq_M $\lvert e\rvert$	Δq (O $\rightarrow$ C) $\lvert e\rvert$	$\Delta G^{\ddagger}$ (eV)	O–C–O (°)
Zr_6	+0.004	+0.009	−0.143	0.000	0.52	155.8
Ti_1Zr_5	+0.044	+0.024	+0.010	0.000	0.21	149.5
Ti_2Zr_4	+0.045	−0.030	+0.012	+0.030	0.30	150.4

Note: Δq values were obtained from Mulliken charge analysis, where $\Delta q = q$(TS) $- q$(ADS). The adsorption state (ADS) and the transition state (TS) correspond to the OH-assisted pathway. Positive Δq_$C_{(CO_2)}$ denotes charge accepted by the CO_2 carbon, while negative Δq_$O_{(OH)}$ indicates electron donation from the hydroxyl oxygen. Δq_M represents the change on the open Zr/Ti center; where a positive value indicates electron depletion and enhanced electrophilicity. Δq (O $\rightarrow$ C) represents the donation magnitude (≥ 0).

For Ti_2Zr_4, the –OH ligand binds directly to Ti, enhancing O $\rightarrow$ C charge transfer ($0.03|e|$), shortening the Ti–$O_{(OH)}$ to 2.04 Å (*vs.* $>$2.15 Å for Zr–$O_{(OH)}$), and yielding a short $O_{(OH)}$–C distance (1.88 Å) that stabilizes the transition state (E_a = 0.31 eV). Overall, Ti incorporation enhances metal–oxo polarization, strengthens OH$\cdots$$CO_2$ interaction, and promotes facile CO_2 activation.

After the transition state, node-bound bicarbonate (*HCO_3) is formed with relative energies of 0.26, 0.33, and 0.33 eV for Zr_6, Ti_1Zr_5, and Ti_2Zr_4, respectively. The subsequent hydrogenation of *HCO_3 can proceed by (i) protonation at the oxygen atom to yield carbonic acid (*H_2CO_3), which readily decomposes into *CO_2 and H_2O, or (ii) carbon protonation to give *OCHO + H_2O. The newly formed species binds to the adjacent Zr/Ti–OH site and stabilizes the intermediates *via* hydrogen bonding. Our calculations show that the formate pathway is thermodynamically preferred: *OCHO is more stable than *H_2CO_3 and (*CO_2 + H_2O) by 2.40 (1.54), 1.41 (0.82), and 1.01 (0.61) eV for Zr_6, Ti_1Zr_5, and Ti_2Zr_4, respectively. These results identify HCO_3 as the true intermediate in CO_2 activation, in line with previous reports on bicarbonate-mediated CO_2 reduction over UiO-66 MOFs[17] and Fe–porphyrin catalysts.[33,34]

These two routes differ fundamentally in proton–electron requirements. Formation of *H_2CO_3 involves one proton–electron pair and oxygen protonation without carbon reduction—a non-reductive acid–base step. Conversely, *OCHO + H_2O formation requires two proton–electron pairs and creates a C–H bond—the true first reduction of CO_2. This explains the lower free energies for the formate route and consistent thermodynamic preference across all nodes. Moreover, the HCO_3 $\rightarrow$ OCHO conversion is slightly more exergonic for Ti-containing

nodes (by $\geq$ 0.2 eV), confirming that Ti enhances both kinetic and thermodynamic driving forces.

As shown in Fig. 3, the competing carboxyl route *COOH + H_2O is $>$ 1 eV less favorable for all systems. Compared with the passive-pathway, the *COOH intermediate in the OH-assisted mechanism is approximately 1 eV more stable (1.31 *vs.* 2.52 eV for Ti_2Zr_4). Subsequent hydrogenation of *COOH produces *CO with relative energies of 2.74, 2.16, and 1.92 eV for Zr_6, Ti_1Zr_5, and Ti_2Zr_4, respectively.

Given the reported band gaps of $\sim$1.7 eV for Zr-MOF-525 and mixed Ti/Zr-MOF-525 and 1.9 eV for free-base TCPP,[16,35] CO formation within $\leq$2.0 eV (for Ti_2Zr_4) is thermodynamically accessible under visible-light excitation, whereas the $\sim$2.5 eV barrier in the passive pathway exceeds the available photoenergy. This correlation suggests that CO generation preferentially occurs *via* the OH-assisted route, especially in Ti-substituted systems. Subsequent hydrogenation of *CO to *CHO or *COH on Ti_2Zr_4 is less favorable than CO desorption, implying that CO is readily released once formed.

Following *OCHO formation, two hydrogenation routes are possible: (i) attack at the carbon to produce *OCH_2O $\rightarrow$ *OCH_2OH, or (ii) attack at the oxygen to generate *HCOOH $\rightarrow$ *CH_2OOH. The *OCH_2OH intermediate then reduces to *OCH_2 with H_2O release. Our calculations reveal that hydrogenation *via* oxygen is thermodynamically more favorable across all systems. The next protonation converts *OCH_2 to *OCH_3, which is more stable than *CH_2OH. Further protonation of *OCH_3 yields *CH_3OH and continued hydrogenation leads to CH_4 formation alongside surface O species that are finally re-hydroxylated, closing the catalytic cycle.

The *OCHO $\rightarrow$ *HCOOH conversion is identified as the potential-determining step, with calculated free-energy changes (ΔG) of 2.10, 0.99, and 0.90 eV for Zr_6, Ti_1Zr_5, and Ti_2Zr_4, respectively (Fig. 3). The desorption energies of the C_1 products were also evaluated and found to be higher than their subsequent hydrogenation energies. For Ti_2Zr_4, *OCH_2 desorption (0.08 eV; relative energy 1.59 eV) is less favorable than its conversion to *OCH_3 (0.52 eV). Similarly, *CH_3OH desorption (1.09 eV) is less stable than final CH_4 formation accompanied by surface –OH regeneration. Overall, Ti substitution and active surface hydroxyls synergistically lower the activation barriers and stabilize key intermediates, thereby driving multi-electron CO_2 reduction beyond the two-electron limit observed on OH-passive surfaces.

In summary, CO_2 photoreduction on mixed Ti/Zr-MOF-525 proceeds most favorably through the OH-assisted formate pathway, where CO_2 activation and the initial hydrogenation yield *OCHO as the key intermediate. The subsequent multi-step hydrogenation follows the sequence *HCOOH $\rightarrow$ *OCH_2OH $\rightarrow$ *OCH_2 $\rightarrow$ *OCH_3 $\rightarrow$ *CH_3OH $\rightarrow$ *OH, accompanied by water formation and regeneration of surface –OH groups. For Ti_2Zr_4, the *OCH_3 $\rightarrow$ *CH_3OH and *OCH_3 $\rightarrow$ *O + CH_4 steps are energetically comparable, allowing both CH_3OH and CH_4 formation. In contrast, for Zr_6 and Ti_1Zr_5, *OCH_3 is more stable than *O, making CH_4 formation less favorable. Ti substitution enhances CO_2 activation, stabilizes key intermediates, and lowers the thermodynamic barriers for deep reduction. Cooperative interactions among open Zr/Ti sites, neighboring hydroxyl groups, and weakly adsorbed water molecules facilitate proton transfer and hydrogen-bond stabilization along the pathway. Overall, Ti-containing nodes exhibit the strongest driving force for multi-electron transfer, enabling selective CH_4 formation under visible-light excitation.

To place the mechanistic results in the context of photocatalysis, we briefly examine the photophysical properties of the mixed Ti/Zr-MOF-525 frameworks. Periodic HSE06//PBE-D3(BJ) calculations yield band gaps of approximately 2.0 eV for all three systems, placing them within the visible-light region and in good agreement with the experimentally reported band gap of $\sim$1.7 eV for mixed Ti/Zr-MOF-525.[16] As shown by the density of states (DOS) analysis (Fig. S3, SI), the highest occupied crystal orbital (HOCO) and lowest unoccupied crystal orbital (LUCO) are largely dominated by porphyrin linker states, while Ti substitution introduces additional Ti 3d states closer to the LUCO, thereby enhancing the electron-accepting character of the metal-oxo node. Although light absorption and charge generation are governed by the extended periodic framework, the subsequent catalytic steps are controlled by the local coordination environment at defective Ti/Zr nodes; accordingly, the cluster-level analysis captures the ground-state energetics that dictate reaction pathways and product selectivity under photocatalytic conditions.

Conclusions

Density functional theory calculations reveal that Ti substitution and node-associated hydroxyl groups jointly govern photocatalytic CO_2 reduction on MOF-525 clusters. Two mechanistic routes were identified: an OH-passive pathway, where the surface –OH group remains inactive and CO_2 reduction terminates at CO and HCOOH, and an OH-assisted pathway, in which a nearby –OH directly attacks the adsorbed CO_2 to form a node-bound *HCO_3 intermediate. The *HCO_3 species acts as the true reactive precursor, undergoing thermodynamically favorable and kinetically accessible conversion to *OCHO and subsequently to CH_4. Ti incorporation strengthens the OH–CO_2 coupling, lowers the activation barriers, and stabilizes intermediates, thereby facilitating deeper multi-electron hydrogenation. Overall, the cooperative effects of Ti substitution and surface hydroxyl groups provide key design guidelines for tuning MOF-525 toward selective CH_4 formation *via* the OH-assisted, bicarbonate-mediated mechanism. These findings underscore the importance of tailoring node composition and surface hydroxyl groups in porphyrinic MOFs to optimize multi-electron CO_2 reduction pathways and control product selectivity.

Author contributions

Thanyaporn Puengpoka: investigation, formal analysis, visualization, and writing – original draft. Jirapat Santatiwongchai: formal analysis, visualization, validation, and writing – reviewing and

editing. Warot Chotpatiwetchkul: investigation, methodology, resources, and writing – reviewing and editing, funding acquisition, and conceptualization. Sareeya Bureekaew: formal analysis, writing – reviewing and editing. Muhammad Saleh: formal analysis, writing – reviewing and editing. Anchalee Junkaew: formal analysis, funding acquisition, writing – reviewing and editing. Sarawoot Impeng: investigation, methodology, validation, formal analysis, resources, writing – reviewing and editing, project administration, funding acquisition, conceptualization (lead), and supervision.

Conflicts of interest

There are no conflicts to declare.

Data availability

The data that support the findings of this study are available from the corresponding author, Dr Sarawoot Impeng, upon reasonable request.

Supplementary information (SI): detailed Gibbs free-energy profiles together with all corresponding optimized structures. See DOI: https://doi.org/10.1039/d5cp04190b.

Acknowledgements

T. P. acknowledges financial support from the School of Science, King Mongkut's Institute of Technology Ladkrabang (Grant No. RA/TA-2566-M-011). W. C. thanks the Thailand Science Research and Innovation (TSRI) and King Mongkut Institute of Technology Ladkrabang for financial support (Grant No. FF68-4776849). We gratefully acknowledge Nanoscale Simulation Laboratory at National Nanotechnology Center (NANOTEC) and NSTDA Supercomputer center (ThaiSC) for providing computational resources. J. S., A. J and S. I. acknowledge financial support from the National Science, Research and Innovation Fund, Thailand Science Research and Innovation (TSRI) (Grant No. FFB680075/0337).

References

1 M. Bui, C. S. Adjiman, A. Bardow, E. J. Anthony, A. Boston, S. Brown, P. S. Fennell, S. Fuss, A. Galindo, L. A. Hackett, J. P. Hallett, H. J. Herzog, G. Jackson, J. Kemper, S. Krevor, G. C. Maitland, M. Matuszewski, I. S. Metcalfe, C. Petit, G. Puxty, J. Reimer, D. M. Reiner, E. S. Rubin, S. A. Scott, N. Shah, B. Smit, J. P. M. Trusler, P. Webley, J. Wilcox and N. Mac Dowell, *Energy Environ. Sci.*, 2018, **11**, 1062–1176.

2 Ž. Kovačič, B. Likozar and M. Huš, *ACS Catal.*, 2020, **10**, 14984–15007.

3 B. Dziejarski, R. Krzyżyńska and K. Andersson, *Fuel*, 2023, **342**, 127776.

4 A. Saravanan, P. Senthil Kumar, D.-V. N. Vo, S. Jeevanantham, V. Bhuvaneswari, V. Anantha Narayanan, P. R. Yaashikaa, S. Swetha and B. Reshma, *Chem. Eng. Sci.*, 2021, **236**, 116515.

5 R. R. Ikreedeegh and M. Tahir, *J. CO2 Utili.*, 2021, **43**, 101381.

6 M. Li, H. Zhang, C. Li, F. Lang, S.-W. Yao, J. Pang and X.-H. Bu, *Prec. Chem.*, 2025, **3**, 424–450.

7 E. Gong, S. Ali, C. B. Hiragond, H. S. Kim, N. S. Powar, D. Kim, H. Kim and S.-I. In, *Energy Environ. Sci.*, 2022, **15**, 880–937.

8 M. Khan, Z. Akmal, M. Tayyab, S. Mansoor, A. Zeb, Z. Ye, J. Zhang, S. Wu and L. Wang, *Carbon Capture Sci. Technol.*, 2024, **11**, 100191.

9 A. Abedi, F. Norouzi and V. Amani, *J. Mater. Chem. A*, 2025, **13**, 23377–23417.

10 X. Zhang, Z. Liu, B. Shao, Q. Liang, T. Wu, Y. Pan, Q. He, M. He, L. Ge and J. Huang, *Small Methods*, 2025, **9**, 2402096.

11 H. Wu, R. Liu, D. Li and Y. H. Ng, *Nano Mater. Sci.*, 2025, DOI: 10.1016/j.nanoms.2024.12.003.

12 H.-Q. Xu, J. Hu, D. Wang, Z. Li, Q. Zhang, Y. Luo, S.-H. Yu and H.-L. Jiang, *J. Am. Chem. Soc.*, 2015, **137**, 13440–13443.

13 H. Zhang, J. Wei, J. Dong, G. Liu, L. Shi, P. An, G. Zhao, J. Kong, X. Wang, X. Meng, J. Zhang and J. Ye, *Angew. Chem., Int. Ed.*, 2016, **55**, 14310–14314.

14 J. Jin, *New J. Chem.*, 2020, **44**, 15362–15368.

15 R. Hariri and S. Dehghanpour, *Appl. Organomet. Chem.*, 2021, **35**, e6422.

16 W.-Y. Gao, H. T. Ngo, Z. Niu, W. Zhang, Y. Pan, Z. Yang, V. R. Bhethanabotla, B. Joseph, B. Aguila and S. Ma, *ChemSusChem*, 2020, **13**, 6273–6277.

17 Y. He, C. Li, X.-B. Chen, Z. Shi and S. Feng, *ACS Appl. Mater. Interfaces*, 2022, **14**, 28977–28984.

18 S. Mandal, R. Leiter, J. Biskupek, U. Kaiser and A. Pannwitz, *ChemSusChem*, 2025, **18**, e202500372.

19 A. Ortega-Guerrero, M. Fumanal, G. Capano, I. Tavernelli and B. Smit, *Chem. Mater.*, 2020, **32**, 4194–4204.

20 W. Morris, B. Volosskiy, S. Demir, F. Gándara, P. L. McGrier, H. Furukawa, D. Cascio, J. F. Stoddart and O. M. Yaghi, *Inorg. Chem.*, 2012, **51**, 6443–6445.

21 A. M. Abdel-Mageed, B. Rungtaweevoranit, S. Impeng, J. Bansmann, J. Rabeah, S. Chen, T. Häring, S. Namuangrak, K. Faungnawakij, A. Brückner and R. J. Behm, *Angew. Chem., Int. Ed.*, 2023, **62**, e202301920.

22 S. Impeng, E. Salaya-Gerónimo, B. Kunkel, S. Bartling, K. Faungnawakij, B. Rungtaweevoranit and A. M. Abdel-Mageed, *J. Mater. Chem. A*, 2024, **12**, 3084–3095.

23 Y. Zhao and D. G. Truhlar, *Theor. Chem. Acc.*, 2008, **120**, 215–241.

24 M. J. Frisch, G. W. Trucks, H. B. Schlegel, G. E. Scuseria, M. A. Robb, J. R. Cheeseman, G. Scalmani, V. Barone, G. A. Petersson, H. Nakatsuji, X. Li, M. Caricato, A. V. Marenich, J. Bloino, B. G. Janesko, R. Gomperts, B. Mennucci, H. P. Hratchian, J. V. Ortiz, A. F. Izmaylov, J. L. Sonnenberg, D. Williams-Young, F. Ding, F. Lipparini, F. Egidi, J. Goings, B. Peng, A. Petrone, T. Henderson, D. Ranasinghe, V. G. Zakrzewski, J. Gao, N. Rega, G. Zheng, W. Liang, M. Hada, M. Ehara, K. Toyota, R. Fukuda, J. Hasegawa, M. Ishida, T. Nakajima, Y. Honda, O. Kitao, H. Nakai, T. Vreven, K. Throssell, J. A. Montgomery, Jr., J. E. Peralta, F. Ogliaro, M. J. Bearpark, J. J. Heyd, E. N. Brothers, K. N. Kudin, V. N. Staroverov,

T. A. Keith, R. Kobayashi, J. Normand, K. Raghavachari, A. P. Rendell, J. C. Burant, S. S. Iyengar, J. Tomasi, M. Cossi, J. M. Millam, M. Klene, C. Adamo, R. Cammi, J. W. Ochterski, R. L. Martin, K. Morokuma, O. Farkas, J. B. Foresman and D. J. Fox, *Gaussian 16*, Gaussian, Inc., Wallingford, CT, 2016.
25 F. Weigend and R. Ahlrichs, *Phys. Chem. Chem. Phys.*, 2005, **7**, 3297–3305.
26 M. Dolg, U. Wedig, H. Stoll and H. Preuss, *J. Chem. Phys.*, 1987, **86**, 866–872.
27 S. Grimme, J. Antony, S. Ehrlich and H. Krieg, *J. Chem. Phys.*, 2010, **132**, 154104.
28 A. V. Marenich, C. J. Cramer and D. G. Truhlar, *J. Phys. Chem. B*, 2009, **113**, 6378–6396.
29 R. F. Ribeiro, A. V. Marenich, C. J. Cramer and D. G. Truhlar, *J. Phys. Chem. B*, 2011, **115**, 14556–14562.
30 G. Luchini, J. Alegre-Requena, I. Funes-Ardoiz and R. Paton, *F1000Res.*, 2020, **9**, 291.
31 A. A. Peterson, F. Abild-Pedersen, F. Studt, J. Rossmeisl and J. K. Nørskov, *Energy Environ. Sci.*, 2010, **3**, 1311–1315.
32 P. Lyu and G. Maurin, *ACS Appl. Nano Mater.*, 2022, **5**, 17750–17757.
33 R. Khakpour, D. Lindberg, K. Laasonen and M. Busch, *ChemCatChem*, 2023, **15**, e202201671.
34 R. Khakpour, K. Laasonen and M. Busch, *Electrochim. Acta*, 2023, **442**, 141784.
35 D. Marsh and L. Mink, *J. Chem. Educ.*, 1996, **73**, 1188–1190.

